JGR Solid Earth

RESEARCH ARTICLE
10.1029/2022JB026309

Defining Continental Lithosphere as a Layer With Abundant Frozen-In Structures That Scatter Seismic Waves

V. Levin[1], S. Lebedev[2,3], J. Fullea[3,4], Y. Li[5], and X. Chen[1]

[1]Rutgers University, Piscataway, NJ, USA, [2]University of Cambridge, Cambridge, UK, [3]Dublin Institute for Advanced Studies (DIAS), Dublin, Ireland, [4]Universidad Complutense de Madrid, Madrid, Spain, [5]Binghamton University, Binghamton, NY, USA

Key Points:

- Beneath eastern North America sharp vertical gradients in seismic properties are pervasive, vary in nature and number, and extend to ~170 km
- Detected gradients reside above the depth to the thermally and mechanically defined lithosphere-asthenosphere boundary
- Continental lithosphere retains pervasive internal layering of density, elastic moduli, and texture, which is mixed out in the asthenosphere

Supporting Information:

Supporting Information may be found in the online version of this article.

Correspondence to:

V. Levin,
vlevin@eps.rutgers.edu

Citation:

Levin, V., Lebedev, S., Fullea, J., Li, Y., & Chen, X. (2023). Defining continental lithosphere as a layer with abundant frozen-in structures that scatter seismic waves. *Journal of Geophysical Research: Solid Earth*, *128*, e2022JB026309. https://doi.org/10.1029/2022JB026309

Received 21 DEC 2022
Accepted 27 JUN 2023

Author Contributions:

Conceptualization: V. Levin, S. Lebedev, J. Fullea
Data curation: Y. Li, X. Chen
Formal analysis: S. Lebedev, J. Fullea, Y. Li, X. Chen
Investigation: V. Levin, J. Fullea
Methodology: S. Lebedev
Software: J. Fullea, X. Chen
Visualization: V. Levin
Writing – original draft: V. Levin, S. Lebedev, J. Fullea

Abstract We investigate the structure of the continental lithosphere by combining two approaches: a systematic survey of abrupt changes in seismic properties detected by *P*-to-*S* converted body waves and an integrated geophysical-petrological inversion for temperature and density in the upper mantle. We refine the global thermo-chemical model WINTERC-G in eastern North America by including detailed regional information on the crust into petrological inversions and combine it with the upper mantle layering beneath eastern North America yielded by anisotropy-aware receiver-function analysis. Eastern North America's Archean, Proterozoic and Paleozoic lithospheres show an excellent agreement between the depth to the 1,300°C isotherm that bounds the lithosphere and the depth range where converted waves detect abrupt changes in seismic properties. Boundaries with these abrupt changes reside within the rigid mechanical lithosphere and are uncommon in the convecting mantle beneath it. The boundaries include both impedance increases and decreases with depth, as well as anisotropy changes, and must have developed over the course of the assembly and evolution of the lithosphere. In the asthenosphere below, such heterogeneities appear to have been largely mixed out by convection. The existence of abundant interfaces with diverse origin can account for the commonly observed scattered signals from within the continental lithosphere and presents an alternative to the end-member concept of the mid-lithospheric discontinuity as a ubiquitous feature with a uniform origin. Generally, we can define continental lithosphere as a region of conductive heat transport and steep geotherm that is characterized by pervasive internal layering of density, elastic moduli and texture.

Plain Language Summary The outer shell of the Earth called the lithosphere is defined most generally as a layer of rigid colder material overlying a warmer and weaker asthenosphere below. Within the lithosphere heat is conducted from the interior to the outside, resulting in a characteristic increase in temperature with depth. The region below it convects on geological (millions of years) time scale and has a different depth dependence of temperature. In this contribution we use two definitions of the lithosphere to estimate its vertical extent beneath a region of North American continent where lithosphere formed between 3 and 0.3 Ga ago. We detect abrupt changes in physical properties in the upper layers of the Earth using seismic waves from distant earthquakes. We perform a joint inversion of geophysical and petrological constraints to derive temperature profiles with depth. Boundaries scattering seismic waves are detected throughout the depth range where temperature is below 1,300°C. The deepest scattering boundaries are close to this depth in areas where lithosphere formed within the last billion years. In the oldest part of the continent the deepest boundaries are ~50 km above the temperature of 1,300°C, confirming long-recognized difference of such ancient lithosphere.

1. Introduction

The lithosphere is the rigid outermost layer of the Earth where mantle flow is absent due to its high viscosity, and the geotherm is controlled by heat conduction (e.g., Barrell, 1914; Daly, 1940; McKenzie et al., 2005). In the sub-lithospheric upper mantle, flow and stirring take place due to the relatively low viscosity values, leading to a geotherm that is typically close to an adiabatic temperature gradient in the range 0.4–0.6 K/km (e.g., Katsura et al., 2010). The Earth's continental lithosphere is a product of processes spanning the bulk of the existence of our planet. Continental lithosphere hosts rocks as old as 4.03 Ga (Bowring & Williams, 1999) and minerals dating to as early as 4.4 Ga (Valley et al., 2014). While the ability of the continents' Archean cores to resist destruction by tectonic and convective forces makes them an invaluable repository of planetary history, their origins and mechanisms of longevity are yet to be fully understood (Bedle et al., 2021; Jordan, 1978; Lee et al., 2011).

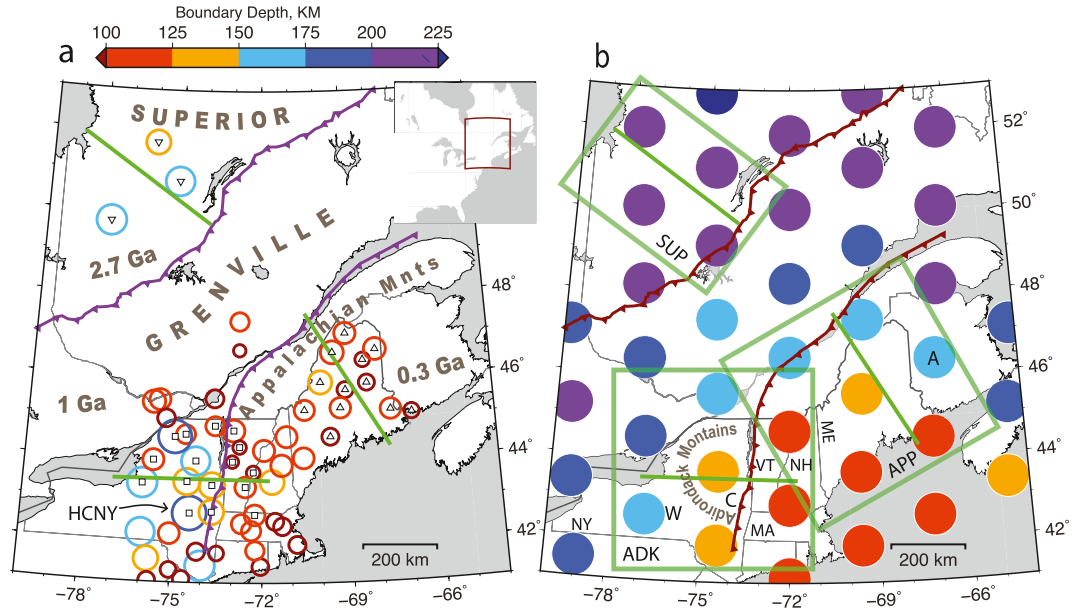

Figure 1. (a) Regional map showing the deepest seismic boundaries detected using *P*-*S* converted waves at numerous locations. Results adapted from X. Chen et al. (2021) and Y. Li et al. (2021). Also shown are names and ages of main tectonic units and locations of seismic stations used in later figures (triangles and boxes). Circles representing deepest boundaries from which *P*-to-*S* waves are detected are scaled proportional to boundary depth (see text for details). Data from seismic station HCNY are used in the example of receiver function (RF) analysis. (b) Values of lithosphere-asthenosphere boundary (LAB) depth in an updated WINTERC-G model (Fullea et al. (2021) inverted with additional constraints in the crust and a different regularization for the thermal buffer thickness, see Section 5.1 for details) plotted over the outlines of tectonic units. US. states and Adirondack Mountains are labeled. Three nodes used as examples of data fit are marked (C, Adirondacks Center; W, Adirondacks West; A, Appalachians). Circle size chosen for nodes of the WINTERC-G model is arbitrary. Green lines correspond to horizontal dimensions of vertical cross-sections shown in Figures 5 and 6. Green boxes (labeled) enclose groups of seismic stations (triangles, boxes) and nodes of WINTERC-G model used for comparisons with results of RF analysis. LAB depth in the original model is shown in Figure S1 in Supporting Information S1.

The definition of the lithosphere-asthenosphere boundary (LAB) was recognized as one of the Grand Challenges of seismology over a decade ago (Lay et al., 2009), and numerous open questions about it remain (Rychert et al., 2020). Studies of the internal structure of the lithosphere provide a progressively more nuanced view of it (cf. Yuan and Romanowicz, 2018), but the emerging complexity is puzzling and does not have consensus explanations.

Recently, it has become possible to calculate multi-parameter physical models of the lithosphere and underlying upper mantle directly from surface-wave and other geophysical data, by means of inversions using integrated geophysical-petrological methods (e.g., Afonso, Fullea, Griffin, et al., 2013; Afonso, Fullea, Yang, et al., 2013; Afonso et al., 2022; Altoe et al., 2020; Fullea et al., 2012). With temperature and composition of the upper mantle and the lithospheric thickness being the inversion parameters, steady-state geotherms and synthetic geophysical observables are calculated directly from them. This forms the basis for a self-consistent inversion that can fit seismic and other data closely and extract highly complete structural information from them. The recently published multi-parameter model WINTERC-G (Fullea et al., 2021) based on such integrated methodology contains the lithospheric thickness, temperature and composition for the entire globe.

The purpose of this paper is to reconcile thermo-chemical mapping of the lithospheric thickness with evidence from seismic-wave reflectivity (i.e., strong vertical gradients in seismic properties) in the upper mantle—and to establish what they are telling us about the structure and dynamics of the lithosphere and asthenosphere. We refine the WINTERC-G model in eastern North America region (Figure 1) by including detailed regional information on the crustal structure into updated petrological inversions. The choice of the region to perform this comparison is driven by the recently published surveys of upper mantle layering beneath eastern North America by Y. Li et al. (2021) and X. Chen et al. (2021) that reported both impedance and anisotropy gradients at a large set of locations spanning a broad range of lithospheric ages, from Archean to Paleozoic. To the best of our knowledge this is the only region where such a detailed receiver function (RF) study has been attempted to date.

Our principal finding is that over a broad region of eastern North America all discontinuities in seismic properties detected by RF analysis reside within the mechanical lithosphere, and none do in the convecting mantle below. The match between the depths of detectable lithospheric layering and the estimate of lithospheric thickness is very close in Paleozoic and Proterozoic regions, where we find scattering boundaries throughout the depth range dominated by conductive heat transport that defines the lithosphere in the WINTERC-G model. Beneath the Archean-aged Superior Province we detect discontinuities down to ∼170 km while the estimate of lithospheric thickness is at least 50 km larger. This apparent seismic transparency of the lowermost part of cratonic lithosphere is consistent with petrological, heat flow, gravity and seismic characterizations (Bedle et al., 2021; Forte & Claire Perry, 2000; Jordan, 1978; Lee et al., 2011) suggesting that cratons are systematically different from continental regions formed in more recent times.

2. Constraints and Uncertainties in Defining the Lithosphere

Studies of seismic wave travel times from large explosions reveal the presence of numerous scatterers and discontinuities with abrupt property changes across them within the continental lithosphere, characterized by velocity decreases (e.g., Thybo & Perchuć, 1997) or increases (e.g., Hales, 1969) in the 80–150 km depth range. Long seismic traverses across Eurasia using exceptionally large controlled sources (e.g., Priestley et al., 1994; Solodilov, 1997) show evidence for multiple discontinuities in seismic velocity within the upper mantle, down to depths of ∼200 km. Both increases and decreases in velocity are inferred across these discontinuities, with up to three low-velocity zones being present beneath some regions (e.g., Morozova et al., 1999). The number of discontinuities and their depths vary on a lateral scale of a few hundreds of km.

Mode converted body waves (*P*-to-*S* or *S*-to-*P*) from distant earthquakes form the basis for receiver function (RF) analysis (Ammon, 1991; Owens et al., 1984) widely used for detection and characterization of vertical gradients in seismic impedance (velocity × density) within the upper mantle, in particular the negative gradient expected at the bottom of the lithosphere (Fischer et al., 2010). Using a globally distributed set of seismic observatories, Rychert and Shearer (2009) used *P*-to-*S* RFs to detect prominent downward decreases in impedance in the depth range 80–130 km beneath continental regions. Although in some locations these could be interpreted as the LAB, in cratons the lithosphere is known to be substantially thicker than this from seismic surface-wave dispersion, seismic waveform modeling and magnetotelluric imaging, as well as from diamondiferous kimberlite data (e.g., Boyd et al., 1985; Fullea et al., 2011; Lebedev et al., 2009; Yuan & Romanowicz, 2010). These results thus indicate widespread prominent interfaces within the lithosphere.

Hopper and Fischer (2018) took advantage of the dense uniform grid of the Earthscope Transportable Array to map the largest negative gradient in impedance within the upper mantle of North America with S-to-*P* RFs, finding it between 60 and 120 km. Similar to numerous other studies using RF methods, these investigations yielded seismological observations of strong negative gradients in impedance within the thick continental lithosphere of tectonically older (Proterozoic and Archean) regions (e.g., Forte & Claire Perry, 2000; Lee et al., 2011). The concept of mid-lithospheric discontinuity (MLD) was introduced by Abt et al. (2010) to address the challenge of interpreting observations of discontinuities at depths shallower than the LAB, and numerous studies have since reported one or more MLDs (e.g., Birkey et al., 2021; Calò et al., 2016) beneath continents.

In addition to impedance changes, mantle lithosphere of continents contains boundaries with abrupt vertical gradients in seismic anisotropy across them (e.g., Bostock, 1997; X. Chen et al., 2021; Ford et al., 2016; Levin & Park, 2000; Y. Li et al., 2021; Wirth & Long, 2014). Their detection is contingent on good directional coverage of distant earthquake sources and, with more long-operating seismic sites making their data available, studies of texture layering in subcontinental lithosphere are becoming more common. A frequent finding in these studies is that of multiple boundaries with abrupt seismic property changes across them at depths as large as 180 km, and of lateral variability in the number and nature of these boundaries (Ford et al., 2016; Y. Li et al., 2021).

Both the long seismic traverses and teleseismic observations are, thus, consistent with the presence of numerous discontinuities and scatterers within the lithospheric depth range. Some of them can be attributed to the LAB, and others reside within the lithospheric mantle and have been attributed to an MLD or multiple MLDs in the same locations (e.g., Birkey et al., 2021). Some of the discontinuities within the lithosphere may be due to phase transformations (Hales, 1969). Many others are likely to be due to various structural, compositional and anisotropy interfaces created in the course of the assembly and evolution of the lithosphere (e.g., Calvert et al., 2021; C.

W. Chen et al., 2009; Cook et al., 1999; Levin et al., 2023; Zhao et al., 2022). Such structures are frozen-in and preserved within the mechanically strong lithosphere but are likely to be mixed out in the low viscosity, convecting asthenosphere beneath it.

In order to test this hypothesis, we need to compare upper mantle reflectivity observations with accurate estimates of the thickness of the lithosphere. Such comparison would allow us to assess whether the lithosphere can, indeed, be identified as a reflective layer atop a largely transparent asthenosphere.

Lateral variability in the lithospheric thickness is readily apparent from tomographic models (e.g., Debayle et al., 2016; Priestley et al., 2018; Schaeffer & Lebedev, 2013). Tectonic regionalization based on tomography (Lekic et al., 2011; Schaeffer & Lebedev, 2015) discriminates between lithospheres of different tectonic types (Archean cratons, stable platforms and tectonic continents) based on their overall thickness. Yet, the absolute thickness of the lithosphere, which we need here, is more difficult to determine.

Tomographic inverse problems yield non-unique models and are not formulated to produce solutions compatible with realistic lithospheric geotherms, which makes it difficult to estimate thermal (and hence mechanical) lithospheric thickness from them accurately. The mechanical strength of the lithosphere is due to its relatively low temperature. The bottom of the lithosphere can be defined by an isotherm such that convection occurs at temperatures above it and, thus, at depths below the depth where this temperature is reached (e.g., McKenzie et al., 2005). Using this general approach, lithospheric thickness has been inferred from tomography a posteriori (e.g., Hoggard et al., 2020; Priestley & McKenzie, 2006; Priestley et al., 2018; Steinberger & Becker, 2018) by finding steady-state, conductive lithospheric geotherms most consistent, in some sense, with shear-speed profiles given by a tomographic model at each point. Purely seismological efforts to estimate the lithospheric thickness, using a simplified boxcar velocity structure for the high-velocity lid, were also undertaken, from regional to global scales (e.g., Bartzsch et al., 2011; Pasyanos et al., 2014). Yet, the signal of the lithospheric thickness in the surface-wave data (the primary seismic data type sensitive to the lithospheric thickness) is subtle and can be lost, to a significant extent, in the non-uniqueness of the seismic models being converted to physical ones a posteriori or due to the over-simplification of the shear-speed profile within the lithosphere.

3. LAB Definition in WINTERC-G

WINTERC-G is a **W**aveform tomography and Gravity (satellite geoid and gravity anomalies and gradiometeric measurements) **IN**version model of the **TE**mpe**R**ature and **C**omposition of the lithosphere and the upper mantle down to 400 km depth at global scale (Fullea et al., 2021, https://zenodo.org/record/5771863). WINTERC-G is based upon the integrated geophysical-petrological approach ***LitMod*** (Afonso et al., 2008; Fullea et al., 2009) where all relevant mantle rock physical properties modeled (seismic velocities and density) are computed within a thermodynamically self-consistent framework allowing for a direct parameterization in terms of the temperature and composition of the lithosphere-upper mantle. The temperature field in the model is primarily constrained by surface-wave, Rayleigh and Love fundamental mode dispersion curves from high-resolution global phase-velocity maps with an average grid-knot spacing of 225 km, computed using waveform inversion measurements (Fullea et al., 2021; Lebedev et al., 2005). In WINTERC-G we adopt a thermal definition similar to the one used by other authors assimilating the lithosphere-asthenosphere boundary or LAB to a specific isotherm, 1,300°C in our case (e.g., Crosby et al., 2006; Goes et al., 2020; Priestley & McKenzie, 2006). In this way, we determine the steady-state lithospheric geotherm by solving the 1D heat conduction equation for a temperature- and pressure-dependent mantle thermal conductivity, with boundary conditions of fixed temperature at the surface of the Earth and at the LAB (Afonso et al., 2008; Fullea et al., 2009). Between the lithosphere and the sub-lithospheric mantle, we parameterize a "transition" region (a buffer or boundary layer—equivalent to the "thermal boundary layer" of McKenzie et al., 2005) of variable thickness (typically 5–50 km) where both conduction and convection heat transport are taking place (Fullea et al., 2009, 2012; McKenzie et al., 2005). The base of the thermal buffer is defined by the 1,400°C isotherm.

4. Lithosphere Thickness Inferred From the Study of Layering in Seismic Properties

RF method assumes that the observed signal from an earthquake may be separated into contributions of the source, the recording instrument, and the path between them (cf. Langston, 1979). In that framework the *P*-to-*S* converted waves forming beneath a seismic station constitute a path contribution and thus a sequence of such S

waves observed after the "parent" *P* wave constitutes a "RF" that characterizes the subsurface beneath the station (e.g., Rondenay et al., 2017). The method further assumes that *P*-to-*S* conversion takes place at boundaries where abrupt changes in impedance, anisotropic velocity, or both take place. Polarities and amplitudes of these mode-converted phases in the RF time series reflect the nature of the changes in seismic properties across the boundaries. In the simplest case of an isotropic impedance change across a horizontal boundary the outcome of *P*-to-*S* conversion is the same for all ray propagation directions. Departures from these conditions such as a dip of the boundary and a directional dependence (anisotropy) of seismic velocity adjacent to the boundary result in systematic variations in converted wave amplitude and polarity with direction of ray propagation (Cassidy, 1992; Levin & Park, 1997). Later sections summarize the methods used to detect and characterize seismic boundaries in the upper mantle of eastern North America. Exhaustive descriptions of methodology may be found in Xie et al. (2020) as well as in studies from which we derive constraints on the lithosphere layering discussed in this paper (X. Chen et al., 2021; Y. Li et al., 2021).

Regional surveys using RF analysis identify abrupt sub-horizontal boundaries in seismic properties at different depths. In our study, these boundaries may represent changes in impedance, changes in anisotropic component of velocity, or both. Significantly, boundaries reported in the upper mantle of eastern North America by Y. Li et al. (2021) and X. Chen et al. (2021) can be detected by seismic body waves with periods ∼2 s. These boundaries represent vertical gradients in seismic properties over distances no larger than $\sim 0.6 \times \lambda$, where λ is wavelength. Assuming $V_s = 4.5$ km/s in the upper mantle, the vertical dimension of these boundaries is $0.6 \times 2 \times 4.5 = 5.4$ km or less (Levin et al., 2016). At the same time, the lateral extent of boundaries detected from majority of wave propagation directions may be evaluated as a function of depth of the boundary and the ray incidence angle. As shown in Y. Li et al. (2021), the radius of the P-S RF footprint is $R = \sim 0.25$ H, or 25 km at 100 km depth.

Assuming that vertically abrupt (few km) and laterally extensive (few tens of km) boundaries in the upper mantle are much more likely to be within the rigid lithosphere than in the viscous flowing asthenosphere we use the deepest boundary detected beneath a seismic station to define the smallest possible thickness of the lithosphere.

5. Methods

5.1. Integrated Geophysical-Petrological Modeling

To illustrate the lithospheric and upper mantle structure from the integrated geophysical-petrological inversion defining WINTERC-G model we present three example columns from Adirondack Mountains at the south-eastern edge of the Proterozoic Grenville Province and the Paleozoic Appalachian Orogen (Figure 2; see Figure 1 for locations). The primary constraint for the geotherm (and, hence, lithospheric thickness) in WINTERC-G are the phase-velocity data for Love and Rayleigh surface waves (mostly sensitive to V_s variations) and, to a lesser extent, surface heat flow and elevation (isostasy). The surface wave data consists of Rayleigh and Love fundamental mode phase-velocity dispersion curves obtained by the Automated Multimode Inversion (Lebedev et al., 2005) of the waveforms of >25,000 earthquake worldwide (Fullea et al., 2021; Figure S2 in Supporting Information S1). Seismic velocities and density in WINTERC-G are computed, through a self-consistent thermodynamic framework, as a function of the fundamental or primary parameters: pressure, temperature and bulk chemical composition (e.g., Afonso et al., 2008; Connolly, 2005; Fullea et al., 2009, 2021; Khan, 2016; Khan et al., 2007; Kuskov et al., 2014).

Synthetic phase velocity dispersion curves for the model columns in WINTERC-G are computed from the V_s, V_p, and density vertical profiles (after including corrections for attenuation, partial melting and radial anisotropy, cf. Fullea et al., 2021) using a version of the MINEOS modes code (Masters et al., 2011) adapted for the traveling wave decomposition, appropriate for surface waves (Nolet, 2008). Synthetic surface heat flow values are computed from the temperature gradient at the surface of the model and the crustal thermal conductivity in each model column. The predicted surface elevation, under the local isostasy assumption, depends on the vertically integrated crustal and lithospheric mantle densities in the model. Sub-lithospheric temperatures, from the bottom of the transition/buffer zone down to 400 km, are obtained from the inversion of the surface wave data. The geotherm is parametrized by the temperature at three equally spaced depths from the base of the thermal buffer to the top of the transition zone at 400 km. Sub-lithospheric temperatures are vertically regularized depending on the lithosphere and thermal buffer thickness by constraining the excursion from a reference adiabatic gradient of 0.5 K/km (only <100 K are allowed).

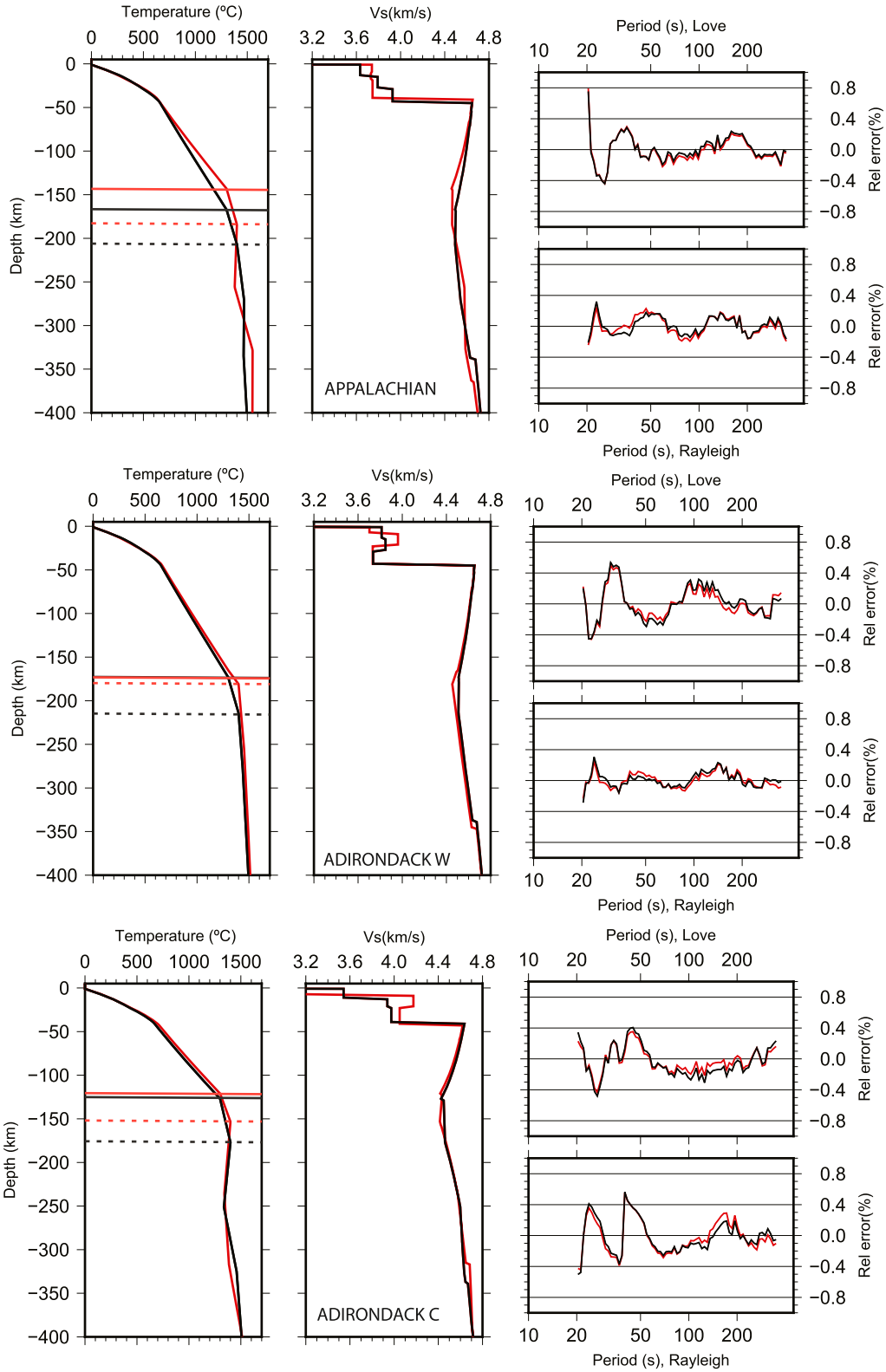

Figure 2.

In this work we modify the original WINTERC-G scheme to implement a more flexible parametrization of the thermal buffer allowing for a gradual transition from the conductive lithosphere to the convective sub-lithosphere. We also include prior information on crustal V_p from controlled source experiments. The inversion for V_s in the crust is set to limit the resulting V_p/V_s ratios within predefined boundaries (1.5–2.1 in the upper crust, 1.67–1.93 in the middle and lower crust), and the input V_p values within uncertainties (1 km/s in the upper crust and 0.2 km/s in the middle and lower crust). An extra term in the misfit function weights the differences between the model crustal V_p and density from the inversion and their lithological predictions based on the V_s and V_p/V_s inverted values (Clemente-Gómez et al., 2022). The crustal lithological predictions are based on empirical V_p-V_s and V_p-density relationships from global petrophysical data (Brocher, 2005; Christensen & Mooney, 1995).

To estimate the uncertainty in the lithospheric thickness obtained from the integrated geophysical-petrological modeling we perform sensitivity tests with the following procedure: starting with the best fitting lithospheric thickness value (Z_{LAB_best}) we carry out alternative inversions with its value fixed and modified progressively (e.g., $Z_{LAB\_best} \pm 1$ km, $Z_{LAB\_best} \pm 2$ km, etc.). The procedure continues until the data misfit is increased significantly (>10%) with respect to the best fitting misfit. The LAB depth uncertainties obtained according to this sensitivity test are generally on order of 10 km for the thin lithospheric columns (<80 km) and 10–20 km for a 130–160 km thick lithosphere.

In Figure 2 we show lithospheric and upper mantle structure in three example columns. The LAB depth, as defined by the 1,300°C isotherm, is around 125–130 and 175 km in the columns under the Adirondacks, and 145–170 km in the column in the Appalachians. The thickness of the thermal buffer (and in general, the inner structure of the LAB) is not well resolved with surface wave data as there are trade-offs with the crustal structure and sub-lithospheric temperatures. Therefore, different thermal and structural models are compatible with the seismic observations. Here, we compare two alternative models corresponding to a different regularization for the thermal buffer thickness and additional regional crustal constraints (i.e., V_p from controlled source studies, Tesauro et al. (2014) and references therein). The original WINTERC-G model is characterized, in general, by a thin thermal buffer leading to a warmer mantle in the vicinity of the LAB. The alternative model shows a thicker thermal buffer and, therefore, a colder mantle around the base of the lithosphere and the asthenosphere. The two models can explain the constraining data with similar misfits. For the Appalachian column, the thermal buffer is similar in the two cases (40 km) but the new alternative model shows a deeper LAB (170 km) compared to the original WINTERC-G model (145 km); however, below the buffer, at around 250 km depth, the original WINTERC-G model is colder than the updated model (Figure 2 top). In the two Adirondack mountains columns the thermal buffer thickness varies from 15 km in the original WINTERC-G model to 40–50 km in the new alternative model (Figure 2 middle and bottom). LAB depths values in the global WINTERC-G model are shown in Figure S2 in Supporting Information S1.

5.2. Receiver Function Analysis

Our data set consists of three-component records of teleseismic body waves from earthquakes in a distance range 20–180°, and comprising phases such as direct *P*, Pdiff, PKP, and PKKP. Prior to the analysis, we rotate the three-component seismograms to a coordinate system aligned with the incoming *P* wave ray (Vinnik, 1977; Figure 3) so that compressional waves appear on the *L* component, converted *P-SV* phases on the *Q* component, and converted *P-SH* phases on the *T* component.

RFs are constructed by isolating *S*-polarized waves on *Q* and *T* components that have the same shape as the *L* component record of the "parent" *P* wave. Construction of RF gathers in either backazimuth or epicentral distance (Figure 4) provides means to detect and characterize candidate *P-S* converted phases and reject energy not consistent with their expected behavior. We average all data in a chosen bin (directional or epicentral), and bins are set to overlap by 50% so each earthquake recorded affects two adjacent bins. An RF phase spanning more than two bins is deemed reliable. Results presented in this paper have at least two events per bin. Prior to combining individual records into backazimuth or epicentral bins, we correct all incoming records for their incidence angle, simulating

Figure 2. Results of the inversion for physical state in three columns (see Figure 1 for location). Geotherm (left), shear wave isotropic velocity (middle), residuals (calculated minus observed) for Rayleigh and Love dispersion curves (right). Red and black lines correspond to the original WINTERC-G model and an alternative model with different regularization for the thermal buffer thickness and additional regional crustal constraints (see main text for details). Horizontal solid and dashed lines in the temperature panel mark the lithosphere-asthenosphere boundary ($T = 1{,}300$°C) and bottom of the thermal buffer ($T = 1{,}400$°C) depths respectively. Additional model parameters (density, anisotropy of seismic velocity, attenuation, magnesium number) are shown in Figures S3–S5 in Supporting Information S1.

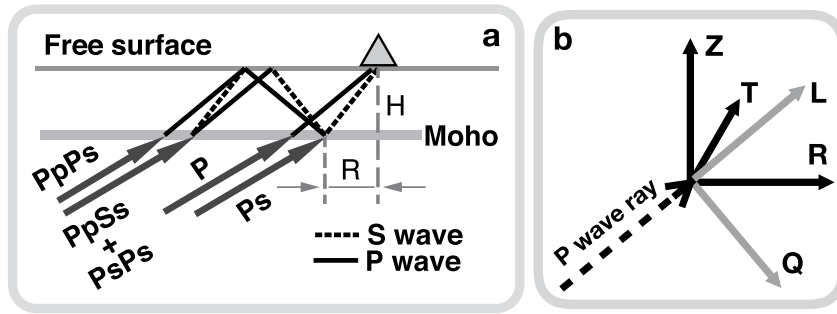

Figure 3. (a) A schematic ray diagram of seismic waves used in the analysis. (b) Coordinate systems used in receiver function analysis: *Z* is vertical, positive up; Radial (*R*) is along the great-circle connecting the source and the receiver, positive from the source to the receiver; Transverse (*T*) is orthogonal to both *R* and *Z*; (*L*) is along the *P* wave ray path, positive from the source to the receiver; (*Q*) is in the vertical plane containing the ray, normal to *L* and positive from the source to the receiver.

vertical incidence. This leads to better alignment of *P*-*S* converted waves in the resulting RF. To focus RF timeseries in the time range where converted waves from our target depth range in the mantle are expected we migrate the time series to the depth of 50 km as described in Park and Levin (2016a). Both move-out corrections and depth migration use site-specific velocity models based on prior studies of the crust and mantle in the region (Levin et al., 2017; Yuan et al., 2014) and the IRIS EARS database (Trabant et al., 2012). Also, these site-specific models are used to predict arrival times for *P*-*S* waves converted from the crust-mantle boundary and the multiply reflected waves within the crust. As discussed below, these predictions (Figure 4) help decide which phases within the observed wavefield should be interpreted. X. Chen et al. (2021) and Y. Li et al. (2021) document specifics of the data sets used here in terms of seismic observatory operation times, numbers of records used, earthquake magnitude ranges included and data availability, and also provide a detailed account of technical steps taken in developing the RFs.

5.2.1. Directional Harmonic Decomposition of RF Wavefield

From theoretical expectations (Park & Levin, 2016b; Xie et al., 2020) polarities and amplitudes of *P*-*S* converted waves vary with direction. At each time step the entire observed RF wavefield can be described by a scaled sum of harmonic functions $\cos(k \times \text{baz})$ and $\sin(k \times \text{baz})$, where baz is the back azimuth of a specific earthquake; $k = 0$ corresponds to the directionally invariant component, and $k = 1$, 2 yield 2-, and 4-lobed variation patterns in 360°. Scalars defining amplitudes of these functions form "harmonic components" of RF wavefield (Figure S6 in Supporting Information S1). Y. Li et al. (2021) introduced the concept of seismic attributes (Bedle, 2019) for these harmonic components. A "Contrast" attribute may be positive or negative when directionally invariant component has a clear phase with corresponding polarity. If a phase is observed on directionally variable components only, the Contrast attribute is "undefined".

For the 50–200 km depth range we investigate, a preferred choice of mechanism for the directional variation in *Q* and *T* component RF timeseries (Figure 4) is seismic anisotropy. Seismic boundaries detected using *P*-*S* converted waves span an area enclosed by the base of the cone of rays passing through the target depth. Y. Li et al. (2021) show the ray cone radius to be $R \sim 0.25H$ where *H* is depth (Figure 3). At 50 km a converting boundary is at least 25 km across, at 150 km is 75 km across, etc. (see Figure 4g). Systematic dips of intra-lithospheric boundaries spanning such distances should result in clear directional variation in the arrival time of the converted wave, on the order of a second or more (e.g., Bianchi et al., 2010). Not finding such variations we deem systematic dips of detected boundaries to be a less plausible origin of harmonic variation in amplitude than effects of seismic anisotropy next to them. Anisotropy with a horizontal symmetry axis yields a pattern described purely by $\sin(2 \times \text{baz})$ and $\cos(2 \times \text{baz})$, while a dipping axis requires contributions with sin(baz) and cos(baz) periodicity. A total amplitude of harmonic components with the same periodicity is computed as a Pythagorean sum of their amplitudes at each time step (Figure 4c) and serves as a measure of energy with specific directional variability at each time step (Xie et al., 2020). Following their association with horizontal and dipping anisotropy-causing fabric, components with $k = 1$ will be referred to as "dipping fabric" (DF) attribute and those with $k = 2$ as "horizontal fabric" (HF) attribute. Experience with synthetic seismograms as well as analytical solutions for *P*-to-*S* conversion in layered anisotropic medium show that under the most general conditions of arbitrarily oriented anisotropic axis both HF and DF components will be needed to capture directional variation of converted wave

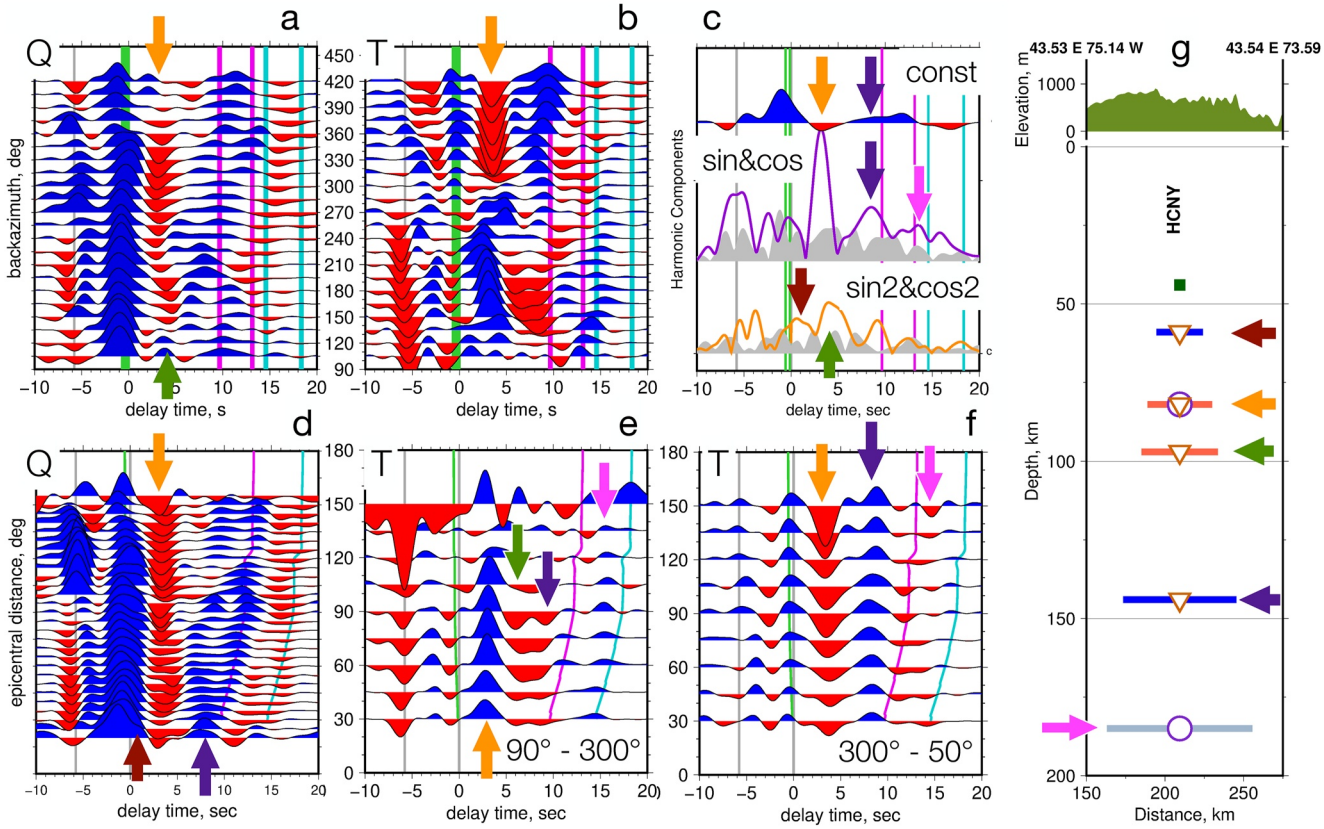

Figure 4. Receiver functions (RFs) and their interpretation for site HCNY in the Adirondack Mountains region of New York (Figure 1), adapted from Y. Li et al. (2021). (a, b) RFs arranged in backazimuth (directions between North and East shown as values in excess of 360); (c) Constant (directionally invariant) component and total amplitudes of directional components with the same periodicity (sin(baz) and cos(baz) and sin(2baz) and cos(2baz)); Gray shading shows error in directional component amplitudes. (d) Epicentral gather of the *Q* component RFs illustrating clear crustal multiples observed between delay times 10 and 17 s; (e, f) Epicentral gathers of *T* component RFs for backazimuth ranges where pulses 3–4 s delay (orange arrow) have consistent polarity. Timeseries are band-limited to 0.02–0.25 Hz. Vertical lines: gray—time at the target depth of 50 km (set to 0 s) and the time of free-surface arrival of the parent *P* wave (−5.8 s); green—time of the Ps wave converted from the Moho computed in a simple model; magenta and cyan–times of the multiply-reflected waves (PpPs, PpSs, and PsPs) computed in the same model, with maximum and minimum times expected for the likely range on incidence angles; (g) Projection of interpreted boundaries onto an E-W striking vertical plane, horizontal size of bars shows the estimated footprint of a cone of rays at the corresponding depth (see Figure 3), colors indicate an increase (blue), decrease (red) or unknown (gray) sense of impedance change, circle indicates strong DF component, triangle–strong HF component at a corresponding boundary. Colored arrows–components of the wavefield interpreted as evidence for distinct boundaries, discussed in Section 5.2.2.

amplitude (Levin & Park, 1997; Park & Levin, 2016a; Xie et al., 2020). The portion of the wavefield that cannot be fit by the above combination of harmonic functions is deemed "unmodelled" and helps assess the reliability of RF waveforms. Xie et al. (2020) use synthetic seismograms to show that reliable DF and HF components have twice the total amplitude of the unmodelled energy at a given time step.

5.2.2. Worked Example of RF Interpretation

To illustrate the process by which RF wavefields are interpreted in terms of boundaries in the upper mantle we present data for site HCNY (Figure 1a) in the Adirondacks where very deep boundaries are detected. Data shown here are for a lower (0.25 Hz) frequency cutoff than same data presented in Figure S24 of Y. Li et al. (2021), while attributes of interpreted boundaries are taken from that study. Phases deemed consistent with boundaries in seismic properties at depth are noted at delay times 0.9, 3.2, 4.7, 9.4, and 13.5 s, corresponding to depths 59, 82, 97, 144, and 185 km. We estimate the accuracy of picking arrival times in our data as 0.1 s, which is equivalent to ∼1 km in the vertical direction. All depth estimates are made with an assumption of $V_p/V_s = 1.8$ in the upper mantle (cf. Y. Li et al., 2021). A smaller value (e.g., $V_p/V_s = 1.7$) will make all depth estimates systematically larger, with changes proportional to boundary depth reaching an order of 20 km at 170 km.

Phase at 0.9 s (red arrow) appears as a small positive *Q* component pulse indicating an increase in impedance with depth and has clear HF component energy. Its DF component has a high noise level (gray filled waveform

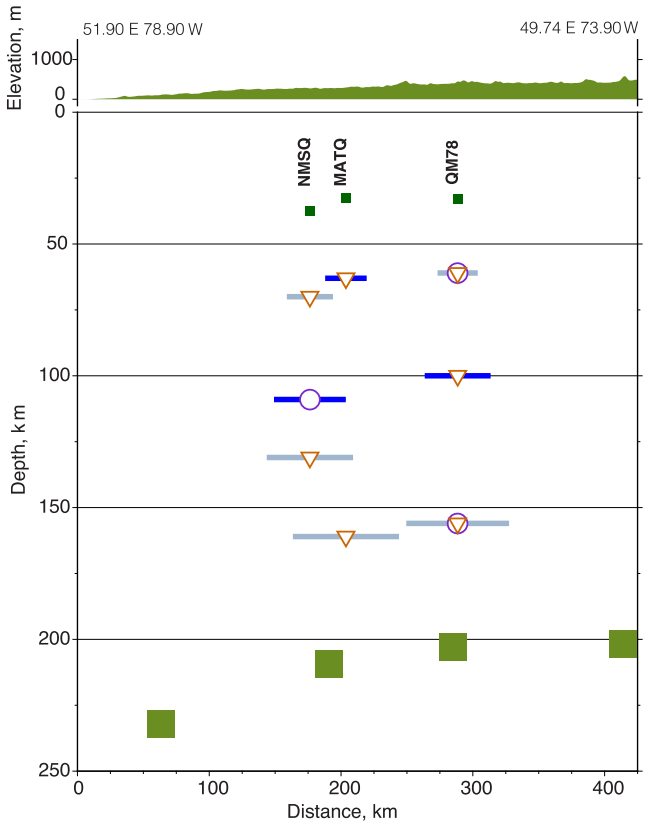

Figure 5. Vertical projection of all converting boundaries within the Superior Craton area of study. Small green boxes show crustal thickness from Levin et al. (2017). Individual boundaries detected by receiver function analysis shown as horizontal bars depicting true scale of the footprint at a given depth. Symbols and plotting conventions same as in Figure 4g. Vertical exaggeration of the cross section is 2:1. All RF values adapted from X. Chen et al. (2021). Depths to the bottom of the lithosphere at corresponding nodes of the WINTERC-G model (Figure 1b) are shown by large green boxes. Thermal buffer extends beyond the bottom of the figure.

in Figure 4c). Phase at 3.2 s (orange arrow) has a clear negative Q component indicating a drop in impedance with depth (Figures 4a and 4d) that is directionally invariant (Figure 4c), and a very strong T component that is positive from the south (backazimuths 90–300, Figure 4e) and negative from the north (backazimuth 300–50, Figure 4f). Both HF and DF components show strong energy. Phase at 4.7 s (green arrow) may be seen mainly from the south (Figures 4a and 4e) and has clear expression in the HF component (Figure 4c). Phase at 9.4 s (purple arrow) is clearly earlier than the crustal multiples (magenta and cyan lines) and displays a different moveout with epicentral distance (Figures 4c and 4d). It has a positive Q component and clear energy in both DF and HF components. The latest phase at 13.5 s (magenta arrow) is identified primarily on the DF component (Figure 4c) and on the T component, with positive polarity from the south (Figure 4e) and negative from the north (Figure 4f). Our choice to interpret this phase as representing a boundary at great depth is guided by its moveout that is clearly distinct from the crustal multiples. Because the phase is within the expected time window of the multiples we do not assign a sense of impedance change to it. Results of similar analysis and interpretation for numerous locations in eastern North America are published in tabular form as supplements to X. Chen et al. (2021) and Y. Li et al. (2021).

6. Results

In Figure 1a we plot the deepest converting boundaries detected at individual sites investigated by Y. Li et al. (2021) and X. Chen et al. (2021), and compare them to the estimates of LAB depth at the nodes of the alternative WINTERC-G model shown in Figure 1b. Almost everywhere in eastern North America the deepest boundaries detected with mode-converted body waves reside above the LAB depth estimated by geophysical-petrological modeling of surface wave and other data sets. In Paleozoic and Proterozoic regions (Appalachians and Grenville, respectively) the deepest boundaries are close to the estimate of the LAB depth, while in the Archean Superior province the LAB is notably (~50 km) deeper than the deepest boundaries. In a few locations beneath the easternmost part of the Grenville Province the deepest boundaries appear at depths 150–180 km, below the depths of the LAB estimated at nearby nodes.

Figures 5 and 6 illustrate the relationship of upper mantle layering and the estimates of LAB depth for three areas outlined in Figure 1b. In these cross sections all detected seismic boundaries from X. Chen et al. (2021) and Y. Li et al. (2021) that fall within a box are plotted at corresponding depths and at lateral positions projected along one of the transect lines. As discussed in the original publications where constraints on mantle layering were presented, we are confident that all detectable boundaries in the depth range 50–250 km are present. This mode of presentation allows us to show additional attributes of these boundaries, such as their Contrast (positive, negative or neutral) and whether there is anisotropy associated with them (DF and HF attributes). Transect orientations in all three cases are chosen to be approximately orthogonal to the nearest major tectonic boundary (the Superior-Grenville boundary for boxes SUP and APP, and Grenville-Appalachian boundary for box ADK).

LAB depth estimates and depths to the bottom of the thermal buffer for all WINTERC-G nodes falling within a given comparison box are similarly projected onto the vertical plane of the transect. These depths are shown at the coordinates of the corresponding node of the WINTERC-G model, with no attempt to represent the smooth nature of surfaces describing depths to temperatures of 1,300 and 1,400°C. In the Superior province (Figure 5) upper mantle layering is limited to a depth range down to ~170 km only. The boundaries show positive or neutral Contrast attributes, and the majority of the detected boundaries have HF attributes, suggesting near-horizontal rock fabric.

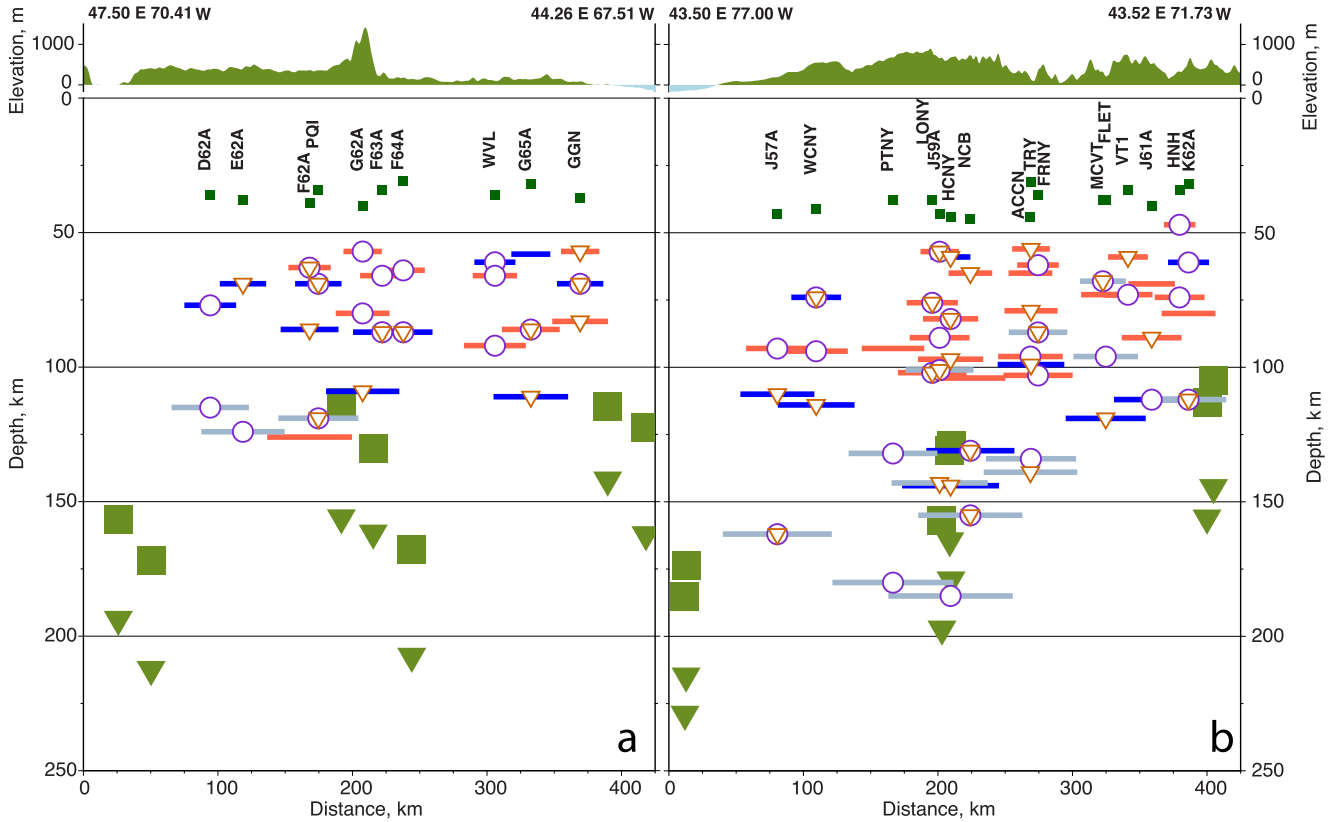

Figure 6. Vertical projections of crustal thickness, receiver function (RF) converting boundaries, and depths to the bottom of the lithosphere at the corresponding WINTERC-G nodes (Figure 1b) for the Appalachians (left) and Adirondacks-New Hampshire (right) areas. Symbols and plotting conventions same as in Figure 4g. Vertical exaggeration 2:1. All RF values adapted from Y. Li et al. (2021). Depths to the bottom of the lithosphere at corresponding nodes of the WINTERC-G model are shown by large green boxes, and a corresponding extent of the thermal buffer is shown by green triangles.

In the Appalachians (Figure 6a) seismic boundaries reside above ~130 km and show a broad range of attributes (Contrast values and anisotropy attributes HF and DF) that appear to be distributed throughout the whole depth range. All LAB depth estimates except for one are below the deepest boundary detected with *P-S* converted waves. If the possible range of thermal buffer thickness from the integrated geophysical-petrological modeling is taken into account, the depth to 1,400°C isotherm (lower lithospheric bound) is everywhere larger than depths of boundaries with abrupt gradients in seismic properties detected using RFs.

The region enclosing Proterozoic Adirondack Mountains of eastern Grenville Province and parts of Paleozoic Appalachian Mountains (Figure 6b) presents a clear departure from simple relationships seen in the other two regions. In the central part of the transect a group of seismic boundaries reside at depths 150–180 km, while the estimate of the LAB depth at nearest nodes is 130–160 km. Projecting all detected boundaries onto a transect, we find, in addition to the very deepest boundaries shown in Figure 1, further ones that also reside below the local estimate of the LAB depth. Significantly, all boundaries detected by *P-S* converted waves reside above the depth to 1,400°C, as defined by the thermal buffer in the alternative WINTERC-G model (Figure 1b).

7. Discussion

RFs yield evidence of the presence of sharp impedance contrasts in the upper mantle. Surface wave data are sensitive to the lithospheric structure in relatively broad depth ranges and, inverted in a thermodynamic framework, together with other relevant data, yield the temperature and thickness of the lithosphere. The inherent ambiguity of interpreting velocity profiles extracted from tomographic models in terms of lithospheric thickness or temperature is considerably reduced by means of the integrated geophysical-petrological modeling of surface wave and other data (Fullea et al., 2021). In this work, we updated a region of the WINTERC-G model for eastern North

America, including specific constraints on the crustal structure from the compilation of Tesauro et al. (2014) and allowing for a larger vertical extent of the thermal buffer that separates purely conductive and purely convective regions in the model.

A comparison of Figure 1b and Figure S2 in Supporting Information S1 shows that the values of the LAB depth (i.e., the 1,300°C isotherm) in the alternative model with a thicker thermal buffer for eastern North America are generally larger than those in the original WINTERC-G model (with a thinner thermal buffer in general), especially in the eastern part where an area of abrupt thinning of the lithosphere was present.

This localized thinning of the lithosphere beneath the coastal region of eastern North America is well recognized in all continent-scale models of the upper mantle that rely on surface waves (e.g., Golos et al., 2020; A. Li et al., 2003; Menke & Levin, 2002; Schaeffer & Lebedev, 2014; Schmandt & Lin, 2014; Shen & Ritzwoller, 2016; Van der Lee & Nolet, 1997). Named a "divot" by Fouch et al. (2000), this region of reduced upper mantle shear wave speed has been associated with various lithospheric thickness values on the basis of mode-converted body waves, from as small as ∼60 km (Hopper & Fischer, 2018) to 100 km or larger (Abt et al., 2010; Rychert et al., 2005). The LAB depth values in the updated WINTERC-G model in the "divot" region fall on the larger end of this range (Figure 1b), as do the estimates based on the deepest observed converting boundaries from RFs considered in this study (Figure 1a). Values of lithospheric thickness in 100–125 km range in a region known as the North Appalachian Anomaly (Menke et al., 2016; Schmandt & Lin, 2014) are also consistent with other mantle temperature estimates from surface wave dispersion (e.g., Steinberger & Becker, 2018). An interesting issue raised by these larger estimates of the lithospheric thickness in coastal eastern North America is the nature of the clear downward decreases in shear waves impedance that are the basis of much shallower LAB estimates in this region by, for example, Hopper and Fischer (2018). Notably, we also find numerous instances of downward decrease in impedance in this region, at depths 60–100 km (Figure 6b, also Figure 5 of Y. Li et al., 2021), thus clearly within the thermally conductive lithosphere and suggestive of lithospheric layering. Their origin is not clear and will require additional study.

Melt has a significant impact on both seismic velocities and attenuation. WINTERC-G model accounts for melt effects considering a mantle-peridotitic nominally anhydrous solidus (Katz et al., 2003) and then computing the effects of melt on V_s, V_p, and attenuation according to experimental results (Chantel et al., 2016). A near-solidus, pre-melt contribution is included to linearly smooth out the effect of melt on seismic velocities over a temperature range in the neighborhood of the solidus, in line with laboratory studies suggesting a progressive, V_s-decreasing effect of anelasticity below the solidus temperature (e.g., Takei, 2017; Yamauchi & Takei, 2016) (see Appendix D in Fullea et al., 2021). In our study region the inversion of the surface wave and other data does not require the presence of melt. In other words, the geotherms in our models do not cross the dry peridotite solidus; in the framework of our integrated geophysical-petrological modeling the velocity drop at the LAB is the result of the combined effects of temperature (changing from conductive and steep in the lithosphere to convective and low quasi adiabatic gradient in the asthenosphere below) and pressure (almost monotonically increasing with depth).

Thermobarometric estimates of the (paleo)geotherm from local xenoliths provide independent information to validate geophysical models. In our study region the closest xenolith data is the Renard suite (longitude: −72.2°, latitude: 52.8°) in the Superior craton. The Renard kimberlites (630–640 Ma) have been studied in terms of geochemistry and thermobarometry (Hunt et al., 2012). In Figure S7 in Supporting Information S1 we compare the temperature and pressure (depth) estimates for the Renard xenolith suite with the geotherm in our closest WINTERC-G column (longitude: −72°, latitude: 52°). The lithospheric thickness in our model close to the Renard suite is about 210 km and corresponds well, except for a few outliers, with the independently derived petrological paleogeotherm, suggesting that the lithosphere has remained stable in the eastern Superior craton since the Late Neoproterozoic.

The modified WINTERC-G model (Figure 1b) in eastern North America presented in this paper shows thicker lithosphere and thermal buffer than the original version, leading to a closer match with the distribution of impedance boundaries defined by the RF analysis considered in this work. Virtually all locations where *P*-*S* converted waves detect an abrupt gradient in properties fall above the depth to the 1,300°C isotherm used to define the LAB in WINTERC-G. This holds true even if uncertainties on the order of 20 km in the LAB depth and estimates of converted boundary depths are taken into account (see Sections 5.1, 5.2.2 and Figures 5 and 6). The only exception is found on the easternmost edge of the Grenville Province within the Adirondack mountains, where some

boundaries fall below the LAB depth estimated from surface waves. Yet all the scattering boundaries are above the depth to the temperature of 1,400°C defining the bottom of the thermal buffer in WINTERC-G.

Examining these boundaries (Figure 6b, also Figures 4 and 5 of Y. Li et al., 2021) we note that most of them do not have a Contrast attribute defined. Timing of the *P*-*S* converted phases from depths 150–200 km places them among the intra-crustal multiples (see Figure 4), making the definition of a Contrast attribute problematic. Instead, these boundaries are identified on the basis of their HF and DF attributes that reflect abrupt vertical gradients in anisotropic seismic velocity. The most likely origin of such abrupt changes in rock fabric are shear zones accommodating the deformation either within the lowest part of the lithosphere, or else directly beneath it. An interpretation in terms of sub-lithospheric shear forming in the upper mantle in response to plate motion is an intriguing possibility. However, in the case of boundaries at the eastern edge of the Grenville Province we prefer a more conservative interpretation and view them as being within the lowermost lithosphere. The mismatch between their depths and the estimate of the LAB depth in the WINTERC-G model (Figure 1b) may simply reflect the fact that lateral resolution in the upper mantle inferred from surface waves is coarser than that associated with RF studies.

Significantly, we do not claim that any of the boundaries we detect represent *the* LAB at any of the locations, what we do claim is that these boundaries are *within* the lithosphere, and the LAB as defined by temperature does not have a uniform seismological signature on vertical scales of tens of km, only on a larger scale controlling surface wave dispersion.

In addition to the numerous detections of interfaces within the lithosphere in studies around the world (e.g., Bostock, 1997; Ford et al., 2016; Hales, 1969; Hopper & Fischer, 2018; Lebedev et al., 2009; Levin & Park, 2000; Priestley et al., 1994; Rychert & Shearer, 2009; Solodilov, 1997; Thybo and Perkhuc, 1997; Wirth & Long, 2014; Yuan & Romanowicz, 2010), discontinuities in the sub-lithospheric upper mantle have also been reported. Hua et al. (2020) used longer wavelength *S*-to-*P* converted waves to detect a relatively smooth increase in seismic wave speed with depth between 80 and 150 km beneath Anatolia, interpreted as the bottom of the low-velocity zone beneath the thin lithosphere of that active region. Velocity changes on the order of 10% over vertical distances of a few tens of km are needed to match observed converted phases, a degree of variation we do not expect in our region (see Figure 2). Also, the *X* discontinuity around 300 km depth has been detected, predominantly in locations with relatively hot asthenosphere (e.g., Pugh et al., 2021, 2023; Schmerr et al., 2013). These discontinuities below the lithosphere have been attributed either to phase transformations or to particular mechanisms of heterogeneity created by mantle upwellings and their interactions with the lithosphere. Whereas interfaces due to phase transformations can be long-lived, chemical heterogeneity in the asthenosphere appears to be mixed effectively by convection within it, with the result that the sub-lithospheric upper mantle is largely transparent, compared to the highly reflective mantle lithosphere.

The existence of abundant interfaces with diverse origin within the lithosphere can account for the commonly observed scattered signals from the lithosphere, observed in continents around the world (e.g., Abt et al., 2010; Birkey et al., 2021; Calò et al., 2016). This presents an alternative to the end-member concept of the MLD as a ubiquitous feature with the same origin and the same significance everywhere. The scattered signals are likely to come, instead, from interfaces of different origin, created by diverse processes over the course of the evolution of the lithosphere.

8. Conclusions

Beneath a large part of the North American continent investigated in this study, vertical gradients in seismic properties are pervasive, vary in their nature and number, and extend down to depths of ∼170 km. The deepest detected gradients always reside above the depth to the 1,300°C isotherm that marks the LAB. In younger (Paleozoic and Proterozoic) regions the deepest boundaries are close to the local LAB depth, while in the Archean region the lowermost ∼50 km of the lithosphere lacks detectable scattering boundaries.

We conclude that abrupt changes in seismic properties reside primarily within the thermally defined rigid mechanical lithosphere and are much rarer in the convecting mantle beneath it (Figure 7). Consequently, we can define continental lithosphere as a region of conductive heat transport and steep geotherm that is characterized by pervasive internal layering of density, elastic moduli and texture. This layering records the history of lithosphere's formation and evolution, with density sorting, subduction, internal deformation and delamination all leaving their marks.

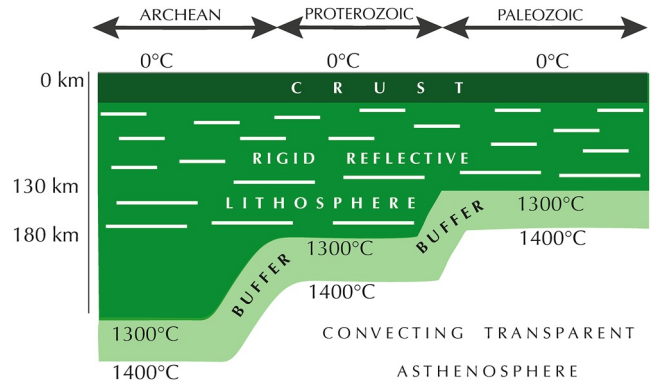

Figure 7. A schematic cartoon summarizing our findings in eastern North America. Conductive rigid mechanical lithosphere bounded by the depth to the temperature of 1,300°C (dark green). The top of convecting asthenosphere (white) is at the depth where temperature reaches 1,400°C. In the region between these depths both conduction and convection of heat take place (light green). Vertical extent of the lithosphere decreases with the age of its formation. Horizontal bars indicate abrupt near-horizontal boundaries in seismic properties detected with receiver functions. Lateral extent of individual boundaries is larger at greater depths. There are no boundaries within the lowermost ∼50 km of the lithosphere consolidated during the Archean. An abrupt change in thickness occurs at the junction of Proterozoic and Paleozoic lithospheres.

Data Availability Statement

Receiver function timeseries were computed using Recfunk21 code package (RU Seismology Group, 2023), available from https://doi.org/10.5281/zenodo.7850744.

Data used in RF analysis work are public and accessible at the IRIS Data Management Center (https://ds.iris.edu/ds/nodes/dmc/). Specific data sets are Albuquerque Seismological Laboratory/USGS (1990, 1994, 2014), IRIS Transportable Array (2003), Lamont Doherty Earth Observatory (LDEO), Columbia University (1970), Menke et al. (2012), Natural Resources Canada (NRCAN Canada) (1975), and Penn State University (2004).

WINTERC-G model is available from https://zenodo.org/record/5771863 (Fullea et al., 2020).

Acknowledgments

We are grateful to reviewers Eva Golos and Cong Li, and the Editor, Michael Bostock, for constructive comments and suggestions. Stimulating discussions during the 2022 SSA conference "Seismic Tomography: What Comes Next?" helped us focus the manuscript. We used GMT (Wessel & Smith, 1991) to draft some of the figures. Receiver function analysis studies were supported by the NSF Earthscope Grant 1735912. We acknowledge support from the European Space Agency (ESA) (projects 3D Earth and 4D Dynamic Earth, Support to Science Element (STSE)), from Science Foundation Ireland (SFI) Grant 13/CDA/2192, and from Grant 16/IA/4598, cofunded by SFI, the Geological Survey of Ireland and the Marine Institute. JF is funded by an Atracción de Talento senior fellowship (2018-T1/AMB/11493) sponsored by Comunidad Autonoma de Madrid (Spain) and a project funded by the Spanish Ministry of Science and Innovation (PID2020-114854GB-C22).

References

Abt, D. L., Fischer, K. M., French, S. W., Ford, H. A., Yuan, H., & Romanowicz, B. (2010). North American lithospheric discontinuity structure imaged by Ps and Sp receiver functions. *Journal of Geophysical Research*, *115*(B09301), 1–24. https://doi.org/10.1029/2009JB006914

Afonso, J. C., Ben-Mansour, W., O'Reilly, S. Y., Griffin, W. L., Salajeghegh, F., Foley, S., et al. (2022). Thermochemical structure and evolution of cratonic lithosphere in central and southern Africa. *Nature Geoscience*, *15*(5), 405–410. https://doi.org/10.1038/s41561-022-00929-y

Afonso, J. C., Fernandez, M., Ranalli, G., Griffin, W. L., & Connolly, J. A. D. (2008). Integrated geophysical-petrological modeling of the lithosphere and sublithospheric upper mantle: Methodology and applications. *Geochemistry, Geophysics, Geosystems*, *9*(5), Q05008. https://doi.org/10.1029/2007GC001834

Afonso, J. C., Fullea, J., Griffin, W. L., Yang, Y., Jones, A. G., Connolly, J. A., & O'Reilly, S. Y. (2013). 3-D multiobservable probabilistic inversion for the compositional and thermal structure of the lithosphere and upper mantle. I: A priori petrological information and geophysical observables. *Journal of Geophysical Research: Solid Earth*, *118*(5), 2586–2617. https://doi.org/10.1002/jgrb.50124

Afonso, J. C., Fullea, J., Yang, Y., Connolly, J. A. D., & Jones, A. G. (2013). 3-D multi-observable probabilistic inversion for the compositional and thermal structure of the lithosphere and upper mantle. II: General methodology and resolution analysis. *Journal of Geophysical Research: Solid Earth*, *118*(4), 1650–1676. https://doi.org/10.1002/jgrb.50123

Albuquerque Seismological Laboratory (ASL)/USGS. (1990). United States National seismic network [Dataset]. International Federation of Digital Seismograph Networks. https://doi.org/10.7914/SN/US

Albuquerque Seismological Laboratory (ASL)/USGS. (1994). New England seismic network [Dataset]. International Federation of Digital Seismograph Networks. https://doi.org/10.7914/SN/NE

Albuquerque Seismological Laboratory/USGS. (2014). Global seismograph network (GSN—IRIS/USGS) [Dataset]. International Federation of Digital Seismograph Networks. https://doi.org/10.7914/SN/IU

Altoe, I., Eeken, T., Goes, S., Foster, A., & Darbyshire, F. (2020). Thermo-compositional structure of the north-eastern Canadian Shield from Rayleigh wave dispersion analysis as a record of its tectonic history. *Earth and Planetary Science Letters*, *547*, 116465. https://doi.org/10.1016/j.epsl.2020.116465

Ammon, C. J. (1991). The isolation of receiver effects from teleseismic P waveforms. *Bulletin of the Seismological Society of America*, *81*(6), 2504–2510. https://doi.org/10.1785/BSSA0810062504

Barrell, J. (1914). The strength of the Earth's crust. *The Journal of Geology*, *22*(7), 655–683. https://doi.org/10.1086/622181

Bartzsch, S., Lebedev, S., & Meier, T. (2011). Resolving the lithosphere–asthenosphere boundary with seismic Rayleigh waves. *Geophysical Journal International*, *186*(3), 1152–1164. https://doi.org/10.1111/j.1365-246X.2011.05096.x

Bedle, H. (2019). Special section: Working with 2D seismic data Seismic attribute enhancement of weak and discontinuous gas hydrate bottom-simulating reflectors in the Pegasus Basin. *New Zealand*, *7*(3), 11–22. https://doi.org/10.1190/INT-2018-0222.1

Bedle, H., Cooper, C. M., & Frost, C. D. (2021). Nature versus nurture: Preservation and destruction of Archean cratons. *Tectonics*, *40*(9), e2021TC006714. https://doi.org/10.1029/2021TC006714

Bianchi, I., Park, J., Agostinetti, N. P., & Levin, V. (2010). Mapping seismic anisotropy using harmonic decomposition of receiver functions: An application to Northern Apennines, Italy. *Journal of Geophysical Research*, *115*(B12), B12317. https://doi.org/10.1029/2009JB007061

Birkey, A., Ford, H. A., Dabney, P., & Goldhagen, G. (2021). The lithospheric architecture of Australia from seismic receiver functions. *Journal of Geophysical Research: Solid Earth*, *126*(4), e2020JB020999. https://doi.org/10.1029/2020JB020999

Bostock, M. G. (1997). Anisotropic upper-mantle stratigraphy and architecture of the Slave craton. *Nature*, *390*(6658), 392–395. https://doi.org/10.1038/37102

Bowring, S. A., & Williams, I. S. (1999). Priscoan (4.00–4.03 Ga) orthogneisses from northwestern Canada. *Contributions to Mineralogy and Petrology*, *134*(1), 3–16. https://doi.org/10.1007/s004100050465

Boyd, F. R., Gurney, J. J., & Richardson, S. H. (1985). Evidence for a 150–200-km thick Archaean lithosphere from diamond inclusion thermobarometry. *Nature*, *315*(6018), 387–389. https://doi.org/10.1038/315387a0

Brocher, T. M. (2005). Empirical relations between elastic wavespeeds and density in the Earth's crust. *Bulletin of the Seismological Society of America*, *95*(6), 2081–2092. https://doi.org/10.1785/0120050077

Calò, M., Bodin, T., & Romanowicz, B. (2016). Layered structure in the upper mantle across North America from joint inversion of long and short period seismic data. *Earth and Planetary Science Letters*, *449*, 164–175. https://doi.org/10.1016/j.epsl.2016.05.054

Calvert, A. J., Doublier, M. P., & Sellars, S. E. (2021). Seismic reflections from a lithospheric suture zone below the Archaean Yilgarn Craton. *Nature Communications*, *12*(1), 7245. https://doi.org/10.1038/s41467-021-27516-w

Cassidy, J. F. (1992). Numerical experiments in broadband receiver function analysis. *Bulletin of the Seismological Society of America*, *82*(3), 1453–1474. https://doi.org/10.1785/BSSA0820031453

Chantel, J., Manthilake, G., Andrault, D., Novella, D., Yu, T., & Wang, Y. (2016). Experimental evidence supports mantle partial melting in the asthenosphere. *Science Advances*, *2*(5), e1600246. https://doi.org/10.1126/sciadv.1600246

Chen, C. W., Rondenay, S., Evans, R. L., & Snyder, D. B. (2009). Geophysical detection of relict metasomatism from an Archean (~3.5 Ga) subduction zone. *Science*, *326*(5956), 1089–1091. https://doi.org/10.1126/science.1178477

Chen, X., Levin, V., Yuan, H., Klaser, M., & Li, Y. (2021). Seismic anisotropic layering in the Yilgarn and Superior cratonic lithosphere. *Journal of Geophysical Research: Solid Earth*, *126*(8), e2020JB021575. https://doi.org/10.1029/2020JB021575

Christensen, N. I., & Mooney, W. D. (1995). Seismic velocity structure and composition of the continental crust: A global view. *Journal of Geophysical Research*, *100*(B6), 9761–9788. https://doi.org/10.1029/95jb00259

Clemente-Gómez, C., Fullea, J., & Arnaiz-Rodríguez, M. S. (2022). A new Integrated lithological model of the Iberian crust. In *EGU general assembly 2022, Vienna, Austria, 23–27 May 2022, EGU22-10232*. https://doi.org/10.5194/egusphere-egu22-10232

Connolly, J. A. (2005). Computation of phase equilibria by linear programming: A tool for geodynamic modeling and its application to subduction zone decarbonation. *Earth and Planetary Science Letters*, *236*(1–2), 524–541. https://doi.org/10.1016/j.epsl.2005.04.033

Cook, F. A., van der Velden, A. J., Hall, K. W., & Roberts, B. J. (1999). Frozen subduction in Canada's Northwest Territories: Lithoprobe deep lithospheric reflection profiling of the western Canadian Shield. *Tectonics*, *18*(1), 1–24. https://doi.org/10.1029/1998tc900016

Crosby, A. G., McKenzie, D., & Sclater, J. G. (2006). The relationship between depth, age and gravity in the oceans. *Geophysical Journal International*, *166*(2), 553–573. https://doi.org/10.1111/j.1365-246X.2006.03015.x

Daly, R. A. (1940). *Strength and structure of the Earth*. Prentice-Hall.

Debayle, E., Dubuffet, F., & Durand, S. (2016). An automatically updated S-wave model of the upper mantle and the depth extent of azimuthal anisotropy. *Geophysical Research Letters*, *43*(2), 674–682. https://doi.org/10.1002/2015GL067329

Fischer, K. M., Ford, H. A., Abt, D. L., & Rychert, C. A. (2010). The lithosphere-asthenosphere boundary. *Annual Review of Earth and Planetary Sciences*, *38*(1), 551–575. https://doi.org/10.1146/annurev-earth-040809-152438

Ford, H. A., Long, M. D., & Wirth, E. A. (2016). Midlithospheric discontinuities and complex anisotropic layering in the mantle lithosphere beneath the Wyoming and Superior Provinces. *Journal of Geophysical Research: Solid Earth*, *121*(September), 6675–6697. https://doi.org/10.1002/2016JB012978

Forte, A. M., & Claire Perry, H. K. (2000). Geodynamic evidence for a chemically depleted continental tectosphere. *Science*, *290*(5498), 1940–1944. https://doi.org/10.1126/science.290.5498.1940

Fouch, M. J., Fischer, K. M., Parmentier, E. M., Wysession, M. E., & Clarke, T. J. (2000). Shear wave splitting, continental keels, and patterns of mantle flow. *Journal of Geophysical Research*, *105*(B3), 6255–6275. https://doi.org/10.1029/1999JB900372

Fullea, J., Afonso, J. C., Connolly, J. A. D., Fernandez, M., García-Castellanos, D., & Zeyen, H. (2009). LitMod3D: An interactive 3-D software to model the thermal, compositional, density, seismological, and rheological structure of the lithosphere and sublithospheric upper mantle. *Geochemistry, Geophysics, Geosystems*, *10*(8), Q08019. https://doi.org/10.1029/2009GC002391

Fullea, J., Lebedev, S., Agius, M. R., Jones, A. G., & Afonso, J. C. (2012). Lithospheric structure in the Baikal–central Mongolia region from integrated geophysical-petrological inversion of surface-wave data and topographic elevation. *Geochemistry, Geophysics, Geosystems*, *13*(8), 1–20. https://doi.org/10.1029/2012GC004138

Fullea, J., Lebedev, S., Martinec, Z., & Celli, N. (2020). WINTERC-G: A global, temperature and compositional model of the lithosphere and upper mantle [Dataset]. Version: v5.4. Retrieved from https://zenodo.org/record/5771863

Fullea, J., Lebedev, S., Martinec, Z., & Celli, N. L. (2021). WINTERC-G: Mapping the upper mantle thermochemical heterogeneity from coupled geophysical–petrological inversion of seismic waveforms, heat flow, surface elevation and gravity satellite data. *Geophysical Journal International*, *226*(1), 146–191. https://doi.org/10.1093/gji/ggab094

Fullea, J., Muller, M. R., & Jones, A. G. (2011). Electrical conductivity of continental lithospheric mantle from integrated geophysical and petrological modeling: Application to the Kaapvaal Craton and Rehoboth Terrane, southern Africa. *Journal of Geophysical Research*, *116*(B10), B10202. https://doi.org/10.1029/2011JB008544

Goes, S., Hasterok, D., Schutt, D. L., & Klöcking, M. (2020). Continental lithospheric temperatures: A review. *Physics of the Earth and Planetary Interiors*, *306*, 106509. https://doi.org/10.1016/j.pepi.2020.106509

Golos, E. M., Fang, H., & van der Hilst, R. D. (2020). Variations in seismic wave speed and VP/VS ratio in the North American lithosphere. *Journal of Geophysical Research: Solid Earth*, *125*(12), e2020JB020574. https://doi.org/10.1029/2020JB020574

Hales, A. L. (1969). A seismic discontinuity in the lithosphere. *Earth and Planetary Science Letters*, *7*(1), 44–46. https://doi.org/10.1016/0012-821X(69)90009-0

Hoggard, M. J., Czarnota, K., Richards, F. D., Huston, D. L., Jaques, A. L., & Ghelichkhan, S. (2020). Global distribution of sediment-hosted metals controlled by craton edge stability. *Nature Geoscience*, *13*(7), 504–510. https://doi.org/10.1038/s41561-020-0593-2

Hopper, E., & Fischer, K. M. (2018). The changing face of the lithosphere-asthenosphere boundary: Imaging continental scale patterns in upper mantle structure across the contiguous U.S. With sp converted waves. *Geochemistry, Geophysics, Geosystems*, *19*(8), 2593–2614. https://doi.org/10.1029/2018GC007476

Hua, J., Fischer, K. M., Wu, M., & Blom, N. A. (2020). New approaches to multifrequency Sp stacking tested in the Anatolian region. *Journal of Geophysical Research: Solid Earth*, *125*(11), e2020JB020313. https://doi.org/10.1029/2020JB020313

Hunt, L., Stachel, T., Grütter, H., Armstrong, J., McCandless, T. E., Simonetti, A., & Tappe, S. (2012). Small mantle fragments from the Renard kimberlites, Quebec: Powerful recorders of mantle lithosphere formation and modification beneath the eastern superior craton. *Journal of Petrology*, *53*(8), 1597–1635. https://doi.org/10.1093/petrology/egs027

IRIS Transportable Array. (2003). USArray transportable array [Dataset]. International Federation of Digital Seismograph Networks. https://doi.org/10.7914/SN/TA

Jordan, T. H. (1978). Composition and development of the continental tectosphere. *Nature*, *274*(5671), 544–548. https://doi.org/10.1038/274544a0

Katsura, T., Yoneda, A., Yamazaki, D., Yoshino, T., & Ito, E. (2010). Adiabatic temperature profile in the mantle. *Physics of the Earth and Planetary Interiors*, *183*(1–2), 212–218. https://doi.org/10.1016/j.pepi.2010.07.001

Katz, R. F., Spiegelman, M., & Langmuir, C. H. (2003). A new parameterization of hydrous mantle melting. *Geochemistry, Geophysics, Geosystems*, *4*(9), 1073. https://doi.org/10.1029/2002GC000433

Khan, A. (2016). On Earth's mantle constitution and structure from joint analysis of geophysical and laboratory-based data: An example. *Surveys in Geophysics*, *37*(1), 149–189. https://doi.org/10.1007/s10712-015-9353-z

Khan, A., Connolly, J. A. D., Maclennan, J., & Mosegaard, K. (2007). Joint inversion of seismic and gravity data for lunar composition and thermal state. *Geophysical Journal International*, *168*(1), 243–258. https://doi.org/10.1111/j.1365-246X.2006.03200.x

Kuskov, O. L., Kronrod, V. A., Prokofyev, A. A., & Pavlenkova, N. I. (2014). Thermo-chemical structure of the lithospheric mantle underneath the Siberian craton inferred from long-range seismic profiles. *Tectonophysics*, *615*, 154–166. https://doi.org/10.1016/j.tecto.2014.01.006

Lamont Doherty Earth Observatory (LDEO), Columbia University. (1970). Lamont-Doherty cooperative seismographic network [Dataset]. International Federation of Digital Seismograph Networks. https://doi.org/10.7914/SN/LD

Langston, C. A. (1979). Structure under Mount Rainier, Washington, inferred from teleseismic body waves. *Journal of Geophysical Research*, *84*(B9), 4749–4762. https://doi.org/10.1029/JB084iB09p04749

Lay, T., Aster, R., Forsyth, D., Romanowicz, B., Allen, R. M., Cormier, V. F., et al. (2009). Seismological grand challenges in understanding Earth's dynamic systems. In *Report to the National Science Foundation, IRIS Consortium, 76*.

Lebedev, S., Boonen, J., & Trampert, J. (2009). Seismic structure of precambrian lithosphere: New constraints from broad-band surface-wave dispersion. *Lithos*, *109*(1–2), 96–111. https://doi.org/10.1016/j.lithos.2008.06.010

Lebedev, S., Nolet, G., Meier, T., & Van Der Hilst, R. D. (2005). Automated multimode inversion of surface and S waveforms. *Geophysical Journal International*, *162*(3), 951–964. https://doi.org/10.1111/j.1365-246X.2005.02708.x

Lee, C. T. A., Luffi, P., & Chin, E. J. (2011). Building and destroying continental mantle. *Annual Review of Earth and Planetary Sciences*, *39*(1), 59–90. https://doi.org/10.1146/annurev-earth-040610-133505

Lekic, V., French, S. W., & Fischer, K. M. (2011). Lithospheric thinning beneath rifted regions of Southern California. *Science*, *334*(6057), 783–787. https://doi.org/10.1126/science.1208898

Levin, V., & Park, J. (1997). P-SH conversions in a flat-layered medium with anisotropy of arbitrary orientation. *Geophysical Journal International*, *131*(2), 253–266. https://doi.org/10.1111/j.1365-246X.1997.tb01220.x

Levin, V., & Park, J. (2000). Shear zones in the Proterozoic lithosphere of the Arabian Shield and the nature of the Hales discontinuity. *Tectonophysics*, *323*(3–4), 131–148. https://doi.org/10.1016/S0040-1951(00)00105-0

Levin, V., Servali, A., Van Tongeren, J., Menke, W., & Darbyshire, F. (2017). Crust-mantle boundary in eastern North America, from the (oldest) craton to the (youngest) rift. In G. Bianchini, J.-L. Bodinier, R. Braga, & M. Wilson (Eds.), *The crust-Mantle and lithosphere-asthenosphere boundaries: Insights from xenoliths, orogenic deep sections, and geophysical studies: Geological Society of America special paper 526* (pp. 107–131). https://doi.org/10.1130/2017.2526(06)

Levin, V., van Tongeren, J. A., & Servali, A. (2016). How sharp is the sharp Archean Moho? Example from eastern Superior Province. *Geophysical Research Letters*, *43*(5), 1928–1933. https://doi.org/10.1002/2016GL067729.Received

Levin, V., Yuan, H., & Hynes, A. (2023). Continents never forget: Seismological record of lithospheric deformation 1 billion years ago. *Geological Society, London, Special Publications*, *531*(1), SP531-2022. https://doi.org/10.1144/SP531-2022-164

Li, A., Forsyth, D. W., & Fischer, K. M. (2003). Shear velocity structure and azimuthal anisotropy beneath eastern North America from Rayleigh wave inversion. *Journal of Geophysical Research*, *108*(B8), 2362. https://doi.org/10.1029/2002JB002259

Li, Y., Levin, V., Nikulin, A., & Chen, X. (2021). Systematic mapping of upper mantle seismic discontinuities beneath northeastern North America. *Geochemistry, Geophysics, Geosystems*, *22*(7), e2021GC009710. https://doi.org/10.1029/2021GC009710

Masters, G., Woodhouse, J. H., & Freeman, G. (2011). Mineos v1.0.2 [Software]. Computational Infrastructure for Geodynamics. Retrieved from https://geodynamics.org/cig

McKenzie, D., Jackson, J., & Priestley, K. (2005). Thermal structure of oceanic and continental ithosphere. *Earth and Planetary Science Letters*, *233*(3–4), 337–349. https://doi.org/10.1016/j.epsl.2005.02.005

Menke, W., & Levin, V. (2002). Anomalous seaward dip of the lithosphere–asthenosphere boundary beneath northeastern USA detected using differential-array measurements of Rayleigh waves. *Geophysical Journal International*, *149*(2), 413–421. https://doi.org/10.1046/j.1365-246X.2002.01652.x

Menke, W., Levin, V., & Darbyshire, F. (2012). Deep structure of three continental sutures in eastern North America [Dataset]. International Federation of Digital Seismograph Networks. https://doi.org/10.7914/SN/X8_2012

Menke, W., Skryzalin, P., Levin, V., Harper, T., Darbyshire, F., & Dong, T. (2016). The Northern Appalachian anomaly: A modern asthenospheric upwelling. *Geophysical Research Letters*, *43*(October), 10173–10179. https://doi.org/10.1002/2016GL070918

Morozova, E. A., Morozov, I. B., Smithson, S. B., & Solodilov, L. N. (1999). Heterogeneity of the uppermost mantle beneath Russian Eurasia from the ultra-long-range profile QUARTZ. *Journal of Geophysical Research*, *104*(B9), 20329–20348. https://doi.org/10.1029/1999JB900142

Natural Resources Canada (NRCAN Canada). (1975). Canadian national seismograph network [Dataset]. International Federation of Digital Seismograph Networks. https://doi.org/10.7914/SN/CN

Nolet, G. (2008). A breviary of seismic tomography. In *A breviary of seismic tomography*.

Owens, T. J., Zandt, G., & Taylor, S. R. (1984). Seismic evidence for an ancient rift beneath the Cumberland Plateau, Tennessee: A detailed analysis of broadband teleseismic *P* waveforms. *Journal of Geophysical Research*, *89*(B9), 7783–7795. https://doi.org/10.1029/JB089iB09p07783

Park, J., & Levin, V. (2016a). Anisotropic shear zones revealed by backazimuthal harmonics of teleseismic receiver functions. *Geophysical Journal International*, *207*(2), 1216–1243. https://doi.org/10.1093/gji/ggw323

Park, J., & Levin, V. (2016b). Statistics and frequency-domain moveout for multiple-taper receiver functions. *Geophysical Journal International*, *207*(1), 512–527. https://doi.org/10.1093/gji/ggw291

Pasyanos, M. E., Masters, T. G., Laske, G., & Ma, Z. (2014). LITHO1.0: An updated crust and lithospheric model of the Earth. *Journal of Geophysical Research: Solid Earth*, *119*(3), 2153–2173. https://doi.org/10.1002/2013JB010626

Penn State University. (2004). Pennsylvania State Seismic Network [Dataset]. International Federation of Digital Seismograph Networks. https://doi.org/10.7914/SN/PE

Priestley, K., Cipar, J., Egorkin, A., & Pavlenkova, N. (1994). Upper-mantle velocity structure beneath the Siberian platform. *Geophysical Journal International*, *118*(2), 369–378. https://doi.org/10.1111/j.1365-246X.1994.tb03968.x

Priestley, K., & McKenzie, D. (2006). The thermal structure of the lithosphere from shear wave velocities. *Earth and Planetary Science Letters*, *244*(1–2), 285–301. https://doi.org/10.1016/j.epsl.2006.01.008

Priestley, K., McKenzie, D., & Ho, T. (2018). A lithosphere–asthenosphere boundary—A global model derived from multimode surface-wave tomography and petrology. *Lithospheric discontinuities*, 111–123. https://doi.org/10.1002/9781119249740.ch6

Pugh, S., Boyce, A., Bastow, I. D., Ebinger, C. J., & Cottaar, S. (2023). Multigenetic origin of the X-discontinuity below continents: Insights from african receiver functions. *Geochemistry, Geophysics, Geosystems*, *24*(3), e2022GC010782. https://doi.org/10.1029/2022GC010782

Pugh, S., Jenkins, J., Boyce, A., & Cottaar, S. (2021). Global receiver function observations of the X-discontinuity reveal recycled basalt beneath hotspots. *Earth and Planetary Science Letters*, *561*, 116813. https://doi.org/10.1016/j.epsl.2021.116813

Rondenay, S., Spieker, K., Sawade, L., Halpaap, F., & Farestveit, M. (2017). Glimer: A new global database of teleseismic receiver functions for imaging Earth structure. *Seismological Research Letters*, *88*(1), 39–48. https://doi.org/10.1785/0220160111

RU Seismology Group. (2023). RUseismology/Recfunk21: Recfunk version released 2021:021:21:00 [Software]. v21. https://doi.org/10.5281/zenodo.7850744

Rychert, C. A., Fischer, K. M., & Rondenay, S. (2005). A sharp lithosphere–asthenosphere boundary imaged beneath eastern North America. *Nature*, *436*(July), 542–545. https://doi.org/10.1038/nature03904

Rychert, C. A., Harmon, N., Constable, S., & Wang, S. (2020). The nature of the lithosphere-asthenosphere boundary. *Journal of Geophysical Research: Solid Earth*, *125*(10), e2018JB016463. https://doi.org/10.1029/2018JB016463

Rychert, C. A., & Shearer, P. M. (2009). A global view of the lithosphere-asthenosphere boundary. *Science*, *324*(5926), 495–498. https://doi.org/10.1126/science.1169754

Schaeffer, A. J., & Lebedev, S. (2013). Global shear speed structure of the upper mantle and transition zone. *Geophysical Journal International*, *194*(1), 417–449. https://doi.org/10.1093/gji/ggt095

Schaeffer, A. J., & Lebedev, S. (2014). Imaging the North American continent using waveform inversion of global and USArray data. *Earth and Planetary Science Letters*, *402*, 26–41. https://doi.org/10.1016/j.epsl.2014.05.014

Schaeffer, A. J., & Lebedev, S. (2015). Global heterogeneity of the lithosphere and underlying mantle: A seismological appraisal based on multimode surface-wave dispersion analysis, shear-velocity tomography, and tectonic regionalization. In *The Earth's heterogeneous mantle* (pp. 3–46). Springer. https://doi.org/10.1007/978-3-319-15627-9_1

Schmandt, B., & Lin, F. C. (2014). P and S wave tomography of the mantle beneath the United States. *Geophysical Research Letters*, *41*(18), 6342–6349. https://doi.org/10.1002/2014GL061231

Schmerr, N. C., Kelly, B. M., & Thorne, M. S. (2013). Broadband array observations of the 300 km seismic discontinuity. *Geophysical Research Letters*, *40*(5), 841–846. https://doi.org/10.1002/grl.50257

Shen, W., & Ritzwoller, M. H. (2016). Crustal and uppermost mantle structure beneath the United States. *Journal of Geophysical Research: Solid Earth*, *121*(6), 4306–4342. https://doi.org/10.1002/2016JB012887

Solodilov, L. N. (1997). The GEON centre: 25 years of implementation of PNE in studies of Earth's deep structure. In *Upper mantle heterogeneities from active and passive seismology* (pp. 1–10). Springer. https://doi.org/10.1007/978-94-015-8979-6_1

Steinberger, B., & Becker, T. W. (2018). A comparison of lithospheric thickness models. *Tectonophysics*, *746*(August), 325–338. https://doi.org/10.1016/j.tecto.2016.08.001

Takei, Y. (2017). Effects of partial melting on seismic velocity and attenuation: A new insight from experiments. *Annual Review of Earth and Planetary Sciences*, *40*(1), 447–470. https://doi.org/10.1146/annurev-earth-063016-015820

Tesauro, M., Kaban, M. K., Mooney, W. D., & Cloetingh, S. (2014). NACr14: A 3D model for the crustal structure of the North American continent. *Tectonophysics*, *631*, 65–86. https://doi.org/10.1016/j.tecto.2014.04.016

Thybo, H., & Perchuć, E. (1997). The seismic 8° discontinuity and partial melting in continental mantle. *Science*, *275*(5306), 1626–1629. https://doi.org/10.1126/science.275.5306.1626

Trabant, C., Hutko, A. R., Karstens, R., Ahern, T., & Aster, R. (2012). Data products at the IRIS DMC: Stepping stones for research and other applications. *Seismological Research Letters*, *83*(October), 846–854. https://doi.org/10.1785/0220120032

Valley, J. W., Cavosie, A. J., Ushikubo, T., Reinhard, D. A., Lawrence, D. F., Larson, D. J., et al. (2014). Hadean age for a post-magma-ocean zircon confirmed by atom-probe tomography. *Nature Geoscience*, *7*(3), 219–223. https://doi.org/10.1038/ngeo2075

Van der Lee, S., & Nolet, G. (1997). Upper mantle S velocity structure of North America. *Journal of Geophysical Research*, *102*(B10), 22815–22838. https://doi.org/10.1029/97jb01168

Vinnik, L. P. (1977). Detection of waves converted from P to SV in the mantle. *Physics of the Earth and Planetary Interiors*, *15*(1), 39–45. https://doi.org/10.1016/0031-9201(77)90008-5

Wessel, P., & Smith, W. H. F. (1991). Free software helps map and display data. *Eos, Transactions American Geophysical Union*, *72*(41), 441–446. https://doi.org/10.1029/90EO00319

Wirth, E. A., & Long, M. D. (2014). A contrast in anisotropy across mid-lithospheric discontinuities beneath the central United States—A relic of craton formation. *Geology*, *42*(10), 851–854. https://doi.org/10.1130/G35804.1

Xie, Z., Levin, V., & Wu, Q. (2020). Crustal anisotropy beneath northeastern Tibetan Plateau from the harmonic decomposition of receiver functions. *Geophysical Journal International*, *220*(March), 1585–1603. https://doi.org/10.1093/gji/ggz526

Yamauchi, H., & Takei, Y. (2016). Polycrystal anelasticity at near-solidus temperatures. *Journal of Geophysical Research*, *121*(11), 7790–7820. https://doi.org/10.1002/2016jb013316

Yuan, H., French, S., Cupillard, P., & Romanowicz, B. (2014). Lithospheric expression of geological units in central and eastern North America from full waveform tomography. *Earth and Planetary Science Letters*, *402*, 176–186. https://doi.org/10.1016/j.epsl.2013.11.057

Yuan, H., & Romanowicz, B. (2010). Lithospheric layering in the North American craton. *Nature*, *466*(7310), 1063–1068. https://doi.org/10.1038/nature09332

Yuan, H. & Romanowicz, B. (Eds.). (2018). *Lithospheric discontinuities* (Vol. 239). John Wiley and Sons.

Zhao, L., Tyler, I. M., Gorczyk, W., Murdie, R. E., Gessner, K., Lu, Y., et al. (2022). Seismic evidence of two cryptic sutures in Northwestern Australia: Implications for the style of subduction during the Paleoproterozoic assembly of Columbia. *Earth and Planetary Science Letters*, *579*, 117342. https://doi.org/10.1016/j.epsl.2021.117342